Boundary conditions including sheath effects at a plasma-facing surface

C. A. Ordonez
Department of Physics, University of North Texas, Denton, Texas 76203-0368
(Received 22 July 1996; revised manuscript received 19 September 1996)

It has recently been reported that space-charge saturation occurs adjacent to almost every commonly used plasma-facing material for plasma temperatures above ~50 eV. An electron emission coefficient, defined as the average number of surface-emitted electrons per incident plasma electron, which is near or above unity is responsible for the occurrence of space-charge saturation. With this motivation, a fully kinetic self-consistent theory capable of describing the plasma sheath under conditions of space-charge saturation is developed. The theory is then used to obtain boundary conditions which are suitable for incorporation into computer programs which simulate plasmas. [S1063-651X(97)02602-0]

PACS number(s): 52.40.Hf

I. INTRODUCTION

Computer programs including magnetohydrodynamic (MHD), particle-in-cell (PIC), multifluid, and hybrid codes which simulate plasma processes are being increasingly incorporated in simulations of plasma-based devices. The types of plasma-based devices which can be (or have been) simulated by computer are diverse. Some examples are plasma-filled backward wave oscillators for producing high power microwaves [1], plasma thrusters for space propulsion [2], plasma wind tunnels [3], opening switches including those of the compact toroid type [4], thermionic converters [5], plasma antennas [6], ''table-top'' x-ray lasers [7], electron-plasma-wave particle accelerators [8,9], electron cyclotron resonance ion sources [10,11], waste processors [12], rail guns [13], MHD generators [14], plasma reactors for processing materials [15,16], and fusion reactors [17]. In addition, reentry vehicles and spacecraft in low earth orbit should be mentioned [18,19]. Computer programs which simulate plasma processes often require boundary conditions at plasma-surface interfaces. In this paper, boundary conditions suitable for incorporation into such computer programs are presented which include the effect of the plasma sheath. A plasma sheath forms next to a plasma-surface interface and has a length scale (the Debye length) and a time scale (the inverse electron plasma frequency) which are often smaller than the length and time scales in computer simulations of macroscopic plasma processes. The plasma sheath is both non-neutral and non-Maxwellian and can have a substantial influence on particle and energy transport to a plasma-facing material surface. For example, in Ref. [20] the effect of a plasma sheath on particle and energy flow to an electrically floating plasma-facing surface was reported. The plasma-facing surface bounded a simple magnetic mirror used to confine a collisional hydrogen-isotope plasma. The plasma sheath was found to be responsible for reducing the energy flow to the plasma-facing surface by a factor of 10 compared to that which would occur without the presence of the plasma sheath.

The boundary conditions developed in the work presented here are based on a fully kinetic self-consistent theoretical description of the plasma sheath. Fully kinetic sheath theory was initially developed by modeling the plasma-facing material surface as a particle sink [21]. The theory was later extended to include a surface emitting zero-temperature electrons [22]. Afterward, a surface emitting finite-temperature electrons was taken into account [23]. Fully kinetic sheath theory has been developed by considering planar sources of ions and electrons and evaluating the resulting phase-space distributions for each. This type of fully kinetic planar source approach has also been used for evaluating axial transport in the end region of a tandem mirror [24–28].

Plasma near a solid material surface is normally divided into two regions. The region closest to the material surface has been referred to as the Debye sheath, the collector sheath, or simply, the sheath. The other region has been referred to as the presheath or the source sheath. The two regions together have also been referred to as the sheath. In the present work, the two regions are referred to as the sheath and the presheath. The boundary conditions presented are those that occur at the interface between the presheath and the sheath. (It should be mentioned that by incorporating the boundary conditions at the interface between the presheath and the sheath into a plasma simulation, the presheath region will naturally develop in the simulated plasma.) Depending on the plasma process considered, electrons and ions within the presheath can originate from a combination of mechanisms including plasma diffusion perpendicular and parallel to a magnetic field and ionization of gas atoms and molecules. A fundamental assumption in the fully kinetic planar source approach to sheath theory is that all presheaths can be adequately modeled as a collisionless plasma region which is bounded on one side by a planar source of half-Maxwellian electrons and ions and on the other side by the presheath-sheath interface [21]. This fundamental assumption allows for the plasma description both at the presheath-sheath interface and at any location within the sheath to be self-consistently determined.

Most of the commonly used plasma-facing surface materials have recently been found to have secondary electron emission coefficients near or above 0.9 at moderate edge-plasma temperatures [29]. (An edge plasma is defined at present as a Maxwellian plasma which supplies ions and electrons to a presheath.) For example, the following materials have secondary electron emission coefficients which reach 0.9 at the edge-plasma temperatures indicated (these

values are from Fig. 3 of Ref. [29]): boron, 15 eV; carbon, 42 eV; aluminum, 47 eV; silicon, 29 eV; titanium, 49 eV; iron, 35 eV; copper, 52 eV; molybdenum, 35 eV; and tungsten, 53 eV. The edge-plasma temperature at which the secondary electron emission coefficient reaches ~ 0.9 is important since the onset of space-charge saturation has been found to take place within the plasma sheath when the secondary electron emission coefficient is ~ 0.9 [23]. In Ref. [23], the sheath description is determined self-consistently for a monotonically decreasing potential including the onset of space-charge saturation when the electric field is zero at the wall surface. Reference [23] provides a historical review of sheath theory and a detailed comparison of the fully kinetic approach with other approaches to sheath theory. In the present work, the sheath theory in Ref. [23] is extended by self-consistently determining the sheath properties not only for a monotonically decreasing potential but also for space-charge saturation when the electric field is reversed near the wall surface and a potential minimum occurs within the sheath.

One aspect of fully kinetic sheath theory, which makes it difficult to use, is that evaluation of the sheath and presheath potentials requires a numerical solution to a set of coupled nonlinear equations. Although boundary conditions can be evaluated in closed form, they are in terms of the sheath and presheath potentials. In order to provide for fast computation of the boundary conditions, simple expressions are developed for the sheath and presheath potentials which incorporate fits to numerically calculated values. The problem is considered in a four -dimensional phase space which consists of one spatial and three velocity dimensions with the spatial dimension normal to the plane of the plasma-facing surface. The two velocity dimensions perpendicular to the spatial dimension are symmetric and the theory can, in principle, be reduced from three to two velocity dimensions without loss of information.

The properties of a plasma sheath depend upon a number of things, including plasma composition, ion charge-state distribution, magnetic field angle with respect to the surface normal, plasma flow speed parallel to the surface, and charged-particle emission processes at the surface. The emission processes are affected by such things as surface temperature, composition, cleanness, roughness, electric fields, and magnetic fields. The plasma-facing material surface can be either a current-carrying anode or cathode, or it can electrically float with respect to the plasma. Altogether, a complete theoretical description of a plasma sheath is extremely difficult to achieve and some simplifying approximations are necessary. In the present work, all ions are considered to have the same mass and charge state. The effect of a magnetic field is not taken into account and no plasma flow parallel to the material surface is considered. The sheath is collisionless and bounded at a planar sheath-surface interface by an electrically floating wall which absorbs all incident particles and emits only secondary and thermionic electrons.

In Sec. II the planar source model is used to describe the transport of an individual species of charged particles through three types of electric potential profiles under steady-state, collisionless conditions. In order to avoid having to consider the sign of the charged particles, the theory is developed in terms of potential energy profiles. The three potential energy profiles are illustrated in Fig. 1. In all three cases, a planar particle source is located at x_0 which injects particles with a half-Maxwellian velocity distribution into the spatial region of interest. The spatial region of interest is located between x_0 and x_n and particles which reach $x<x_0$ or $x>x_n$ are considered lost from the region. The role of Sec. II is to present derivations of expressions for phase-space distribution functions and associated densities, fluxes, normalized temperatures, and energy fluxes for the three potential energy profiles in Fig. 1. These expressions allow relations for plasma electrons, plasma ions, and surface-emitted electrons to be written in Sec. III without the need for individual derivations for each particle species. In Sec. IV possible electric potential profiles within the presheath and sheath are evaluated numerically. Three profiles, which are determined self-consistently for a set of example plasma parameters, are shown in Fig. 2. (The three electric potential profiles in Fig. 2 do not correspond to the three potential energy profiles in Fig. 1). The three profiles in Fig. 2 represent the three possible electric potential profiles within a sheath adjacent to an electrically floating, electron-emitting, plasma-facing material surface. The profiles are given in order of increasing

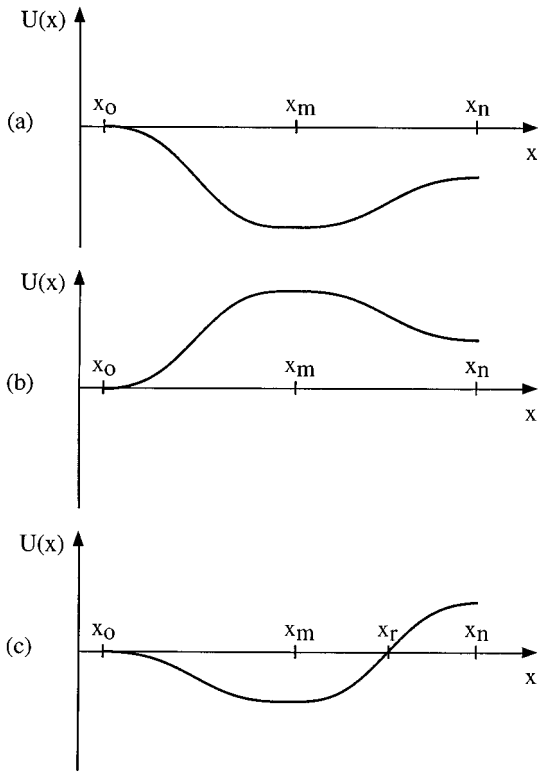

FIG. 1. The particle potential energy profiles considered in Sec. II. A planar source of particles is located at x_0 which emits particles in the positive-x direction. For the potential energy curve shown in (a), $U(x_m)<U(x_n)<U(x_0)$ and all particles originating at x_0 travel past x_n. For the potential energy curve shown in (b), $U(x_0)<U(x_m)$, $U(x_n)<U(x_m)$, and a fraction of the particles originating at x_0 reach a turning point between x_0 and x_m and pass back through x_0. For this potential energy profile, $U(x_n)<U(x_0)$ is also possible. For the potential energy curve shown in (c), $U(x_m)<U(x_0)<U(x_n)$, $U(x_0)=U(x_r)$, and fraction of the particles originating at x_0 reach a turning point between x_r and x_n and pass back through x_0.

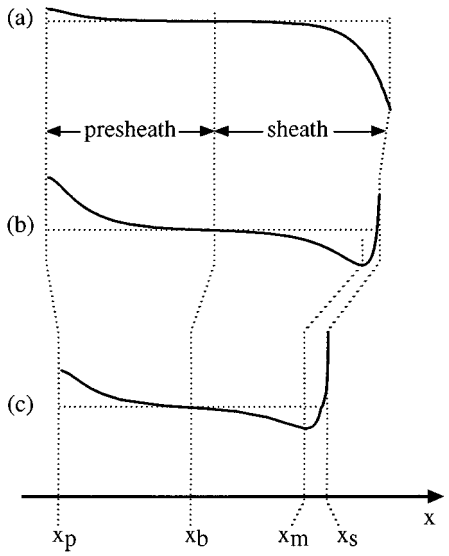

FIG. 2. Illustrations of possible electric potential profiles (solid curves) in the presheath and sheath for (a) no space-charge saturation, (b) space-charge saturation and a surface floating potential which is negative with respect to the edge plasma (at $x \leqslant x_p$), and (c) space-charge saturation and a positive surface floating potential. Although not apparent as a result of the limited resolution of the plots, the electric field is zero at x_p and x_b. The dotted lines are provided to guide the eye.

fluxes of emitted electrons from the plasma-facing material surface. The first profile, Fig. 2(a), is a monotonically decreasing potential which occurs if, for example, the wall surface emits no electrons. The second and third profiles, Figs. 2(b) and 2(c), occur in space-charge saturated sheaths. Notice that with a sufficient flux of emitted electrons, the electrically floating wall gains a positive potential with respect to the plasma. This phenomenon, which is illustrated in Fig. 2(c), has been experimentally observed [30]. For all three profiles, half-Maxwellian plasma electrons and ions are injected at x_p while half-Maxwellian surface-emitted electrons are injected at x_s. It should be mentioned that along with the three profiles in Fig. 2, other electric potential profiles are possible under conditions different from those considered in the present work. For example, if the plasma-facing material surface is a strong emitter of positive ions, a positive space-charge region can be produced which leads to a profile with an electric potential hill.

In Sec. III sets of relations describing the transport of each of the three particle species are given for each of the three electric potential profiles shown in Fig. 2. These sets of relations are determined from the three sets of relations associated with the particle potential energy profiles shown in Fig. 1. The procedure used is illustrated with an example. Suppose surface-emitted electrons, which are injected into the sheath at x_s in Fig. 2, encounter an electric potential profile similar to that in Fig. 2(b). The potential energy profile encountered by these electrons is qualitatively similar to that encountered by particles injected at x_0 into the potential energy profile illustrated in Fig. 1(b). Consequently, the phase-space distribution function, density, flux, normalized temperature, and energy flux derived in Sec. II for the potential energy profile shown in Fig. 1(b) can be written immediately in Sec. III for surface-emitted electrons with only a change in notation. It should be pointed out that the locations x_0 and x_n in Fig. 1 correspond to the locations x_s and x_p in Fig. 2 only when considering surface-emitted electrons. For plasma electrons and plasma ions, the locations x_0 and x_n in Fig. 1 correspond to the locations x_p and x_s in Fig. 2, since plasma electrons and plasma ions are injected at x_p.

In Sec. V boundary conditions at the presheath-sheath interface are given both for sheaths in which space-charge saturation does not occur and for sheaths in which space-charge saturation does occur. Simple expressions for the presheath and sheath potentials are also provided for each of these cases along with an expression which predicts the value of the electron emission coefficient at the onset of space-charge saturation. Section V is self-contained for easy referral. In Sec. VI brief discussions regarding the Child-Langmuir equation and applicability of the work presented are given in consideration of the simplifying assumptions used. This is followed by a concluding summary. Throughout this paper the word ''surface'' refers to a material surface located at the interface between a plasma sheath and a bulk solid.

II. PLANAR SOURCE MODEL

In Fig. 1 a planar particle source is located at x_0 which injects particles in the positive-x direction. The injected-particle velocity distribution function at x_0 is written as $f_0(v_x,v_y,v_z)\Theta(v_x)$ where the Heaviside step function Θ is included to indicate that only particles traveling in the positive-x direction are injected at x_0. As a result of the conservation of energy and momentum, the initial velocity in the x direction of an injected particle at x_0 is related to the particle's velocity in the x direction, v_x, while the particle is located at position x by

$$v_{0x}=\left(v_x^2+\frac{2[U(x)-U_0]}{m}\right)^{1/2}, \tag{1}$$

where $U_0=U(x_0)$ is the particle's potential energy at x_0 and m is the particle mass. The phase-space distribution function for the charged particles must satisfy the steady-state Vlasov equation,

$$mv_x\frac{\partial f_x(x,\mathbf{v})}{\partial x}=\frac{\partial U(x)}{\partial x}\frac{\partial f(x,\mathbf{v})}{\partial v_x}, \tag{2}$$

while taking into account inaccessible regions in phase space. In terms of the injected-particle velocity distribution, the phase-space distribution function given by $f(x,v_x,v_y,v_z)=f_0(v_{0x},v_y,v_z)$ satisfies the steady-state Vlasov equation where v_{0x} is replaced by the right-hand side of Eq. (1).

For the first potential energy profile, Fig. 1(a), the injected particles encounter an asymmetric potential well. In the collisionless limit, all injected particles pass directly through the region between x_0 and x_n and travel only in the positive-x direction. Since all particles must have velocities in the x direction greater than $\sqrt{2[U_0-U(x)]/m}$, the phase-space velocity distribution function is

$$f(x,v_x,v_y,v_z)=f_0(v_{0x},v_y,v_z)\times\Theta\left(v_x-\left(\frac{2[U_0-U(x)]}{m}\right)^{1/2}\right). \tag{3}$$

For the potential energy profile illustrated in Fig. 1(b), particles can be reflected between x_0 and x_m and then travel past x_0 moving in the negative-x direction. Under conditions of complete reflection, $U_m \to \infty$, the injected-particle and reflected-particle parts of the phase-space distribution between x_0 and x_m are symmetric. The only difference for a finite value for U_m is that particles between x_0 and x_m with velocities in the positive-x direction greater than $\sqrt{2[U_m - U(x)]/m}$ are not reflected. Consequently, particles traveling in the negative-x direction are restricted to velocities greater than $-\sqrt{2[U_m - U(x)]/m}$ and the phase-space distribution function which describes the charged particles between x_0 and x_m is

$$f(x,v_x,v_y,v_z) = f_0(v_{0x},v_y,v_z)\Theta\left(v_x + \left(\frac{2[U_m - U(x)]}{m}\right)^{1/2}\right) \quad (x_0 < x < x_m). \quad (4)$$

In the region $x_m < x < x_n$ particles are accelerated in the positive-x direction and are restricted to velocities greater than $\sqrt{2[U_m - U(x)]/m}$. Consequently, the phase-space distribution function in this region is

$$f(x,v_x,v_y,v_z) = f_0(v_{0z},v_y,v_z)\Theta\left(v_x - \left(\frac{2[U_m - U(x)]}{m}\right)^{1/2}\right) \quad (x_m < x < x_n). \quad (5)$$

Notice that the velocity distribution at x_r is the same as at x_0 since $U(x_r) = U(x_0)$. Consequently, the phase-space distribution function for particles between x_r and x_n is similar to that given by Eq. (4). It is

$$f(x,v_x,v_y,v_z) = f_0(v_{0x},v_y,v_z)\Theta\left(v_x + \left(\frac{2[U_n - U(x)]}{m}\right)^{1/2}\right) \quad (x_r < x < x_n). \quad (9)$$

For the three potential energy profiles shown in Fig. 1, the planar particle source located at x_0 is now considered to inject particles having a half-Maxwellian velocity distribution. The half-Maxwellian velocity distribution is

$$f_0(\mathbf{v})\Theta(v_x) = n_0\left(\frac{\beta}{\pi}\right)^{3/2} e^{-\beta v^2}\Theta(v_x), \quad (10)$$

where $\beta = m/(2T_0)$, and n_0 and T_0 are the density and temperature (the latter in energy units) associated with the full-Maxwellian velocity distribution $f_0(\mathbf{v})$. For the potential energy profile shown in Fig. 1(a), the phase-space distribution function is given by Eq. (3). For half-Maxwellian injected particles, the phase-space distribution is

$$f(x,\mathbf{v}) = n_0\left(\frac{\beta}{\pi}\right)^{3/2} e^{-\beta v^2 + \psi_{0x}}\Theta\left(v_x - \left(\frac{\psi_{0x}}{\beta}\right)^{1/2}\right), \quad (11)$$

where $\psi_{0x} = [U_0 - U(x)]/T_0$. The particle density, particle flux, normalized temperature, and energy flux are

$$n = \int f\, d^3v = \tfrac{1}{2} n_0 G_1(\psi_{0x}), \quad (12)$$

The third potential energy profile, Fig. 1(c), causes the particle velocity distribution at any location between x_0 and x_r to occupy two separate velocity regions. One region describes particles moving in the positive-x direction. These particles have a velocity in the x direction greater than $\sqrt{2[U_0 - U(x)]/m}$ and are associated with the phase-space velocity distribution function,

$$f(x,v_x,v_y,v_z) = f_0(v_{0x},v_y,v_z)\Theta\left(v_x - \left(\frac{2[U_0 - U(x)]}{m}\right)^{1/2}\right) \quad (x_0 < x < x_r, v_x > 0). \quad (6)$$

The second region describes particles moving in the negative-x direction. These particles have v_x values between $-\sqrt{2[U_n - U(x)]/m}$ and $-\sqrt{2[U_0 - U(x)]/m}$ and are associated with the phase-space distribution function,

$$f(x,v_x,v_y,v_z) = f_0(v_{0x},v_y,v_z) \times \Theta\left(v_x + \left(\frac{2[U_n - U(x)]}{m}\right)^{1/2}\right) \times \Theta\left(-v_x - \left(\frac{2[U_0 - U(x)]}{m}\right)^{1/2}\right) \quad (x_0 < x < x_r, v_x < 0). \quad (7)$$

Altogether, the phase-space distribution function for particles between x_0 and x_r can be written as

$$f(x,v_x,v_y,v_z) = f_0(v_{0x},v_y,v_z)\left[1 - \Theta\left(v_x + \left(\frac{2[U_0 - U(x)]}{m}\right)^{1/2}\right)\Theta\left(\left(\frac{2[U_0 - U(x)]}{m}\right)^{1/2} - v_x\right)\right] \times \Theta\left(v_x + \left(\frac{2[U_n - U(x)]}{m}\right)^{1/2}\right) \quad (x_0 < x < x_r). \quad (8)$$

$$F=\int v_x f\ d^3v=\frac{n_0}{2\sqrt{\pi\beta}}, \tag{13}$$

$$\frac{T}{T_0}=\frac{2\beta}{3}\left[\frac{\int v^2 f\ d^3v}{\int f\ d^3v}-\left(\frac{\int v_x f\ d^3v}{\int f\ d^3v}\right)^2\right]$$
$$=1+\frac{2\sqrt{\psi_{0x}/\pi}}{3G_1(\psi_{0x})}-\frac{2}{3\pi[G_1(\psi_{0x})]^2}, \tag{14}$$

and

$$Q=\frac{1}{2}\,m\int v^2 v_x f\ d^3v=\frac{(2+\psi_{0x})n_0T_0}{2\sqrt{\pi\beta}}. \tag{15}$$

Here, $G_1(x)=e^x\mathrm{erfc}(\sqrt{x})$, where erfc is the complementary error function.

For the potential energy profile shown in Fig. 1(b), the phase-space distribution function is given by Eqs. (4) and (5). With half-Maxwellian particles injected at x_0, the distribution function, density, flux, normalized temperature, and energy flux are

$$f(x,\mathbf{v})=\begin{cases} n_0\left(\dfrac{\beta}{\pi}\right)^{3/2}e^{-\beta v^2-\psi_{x0}}\Theta\left(v_x+\left(\dfrac{\psi_{mx}}{\beta}\right)^{1/2}\right) & (x_0<x<x_m)\\[2ex] n_0\left(\dfrac{\beta}{\pi}\right)^{3/2}e^{-\beta v^2-\psi_{x0}}\Theta\left(v_x-\left(\dfrac{\psi_{mx}}{\beta}\right)^{1/2}\right) & (x_m<x<x_n), \end{cases} \tag{16}$$

$$n=\begin{cases} \dfrac{1}{2}\,n_0e^{-\psi_{m0}}G_2(\psi_{mx}) & (x_0<x<x_m)\\[2ex] \dfrac{1}{2}\,n_0e^{-\psi_{m0}}G_1(\psi_{mx}) & (x_m<x<x_n), \end{cases} \tag{17}$$

$$F=\frac{n_0e^{-\psi_{m0}}}{2\sqrt{\pi\beta}}, \tag{18}$$

$$\frac{T}{T_0}=\begin{cases} 1-\dfrac{2\sqrt{\psi_{mx}/\pi}}{3G_2(\psi_{mx})}-\dfrac{2}{3\pi[G_2(\psi_{mx})]^2} & (x_0<x<x_m)\\[2ex] 1+\dfrac{2\sqrt{\psi_{mx}/\pi}}{3G_1(\psi_{mx})}-\dfrac{2}{3\pi[G_1(\psi_{mx})]^2} & (x_m<x<x_n), \end{cases} \tag{19}$$

and

$$Q=\frac{(2+\psi_{mx})n_0T_0e^{-\psi_{m0}}}{2\sqrt{\pi\beta}}, \tag{20}$$

where $\psi_{x0}=[U(x)-U_0]/T_0$, $\psi_{mx}=[U_m-U(x)]/T_0$, $\psi_{m0}=[U_m-U_0]/T_0$, and $G_2(x)=e^x\mathrm{erfc}(-\sqrt{x})$.

With half-Maxwellian particles injected at x_0 into the potential energy profile shown in Fig. 1(c), the phase-space distribution function is given by Eqs. (8) and (9). Since the velocity distribution at any location between x_0 and x_r occupies two separate velocity regions, a separate temperature can be associated with each. In order to evaluate the normalized temperature, the phase-space distribution function given by Eq. (6), which describes particles moving in the positive-x direction, is used. The density, flux, and energy flux are found using the phase-space distribution function given by Eqs. (8) and (9). The relations are

$$f(x,\mathbf{v})=\begin{cases} n_0\left(\dfrac{\beta}{\pi}\right)^{3/2}e^{-\beta v^2+\psi_{0x}}\left[1-\Theta\left(v_x+\left(\dfrac{\psi_{0x}}{\beta}\right)^{1/2}\right)\right]\Theta\left(\left(\dfrac{\psi_{0x}}{\beta}\right)^{1/2}-v_x\right)\Theta\left(v_x+\left(\dfrac{\psi_{nx}}{\beta}\right)^{1/2}\right) & (x_0<x<x_r)\\[2ex] n_0\left(\dfrac{\beta}{\pi}\right)^{3/2}e^{-\beta v^2-\psi_{x0}}\Theta\left(v_x+\left(\dfrac{\psi_{nx}}{\beta}\right)^{1/2}\right) & (x_r<x<x_n), \end{cases} \tag{21}$$

$$n=\begin{cases} n_0[G_1(\psi_{0x})-\frac{1}{2}e^{-\psi_{n0}}G_1(\psi_{nx})] & (x_0<x<x_r)\\[2ex] \dfrac{1}{2}\,n_0e^{-\psi_{n0}}G_2(\psi_{nx}) & (x_r<x<x_n), \end{cases} \tag{22}$$

$$F=\frac{n_0e^{-\psi_{n0}}}{2\sqrt{\pi\beta}}, \tag{23}$$

$$\frac{T}{T_0}=\begin{cases}1+\dfrac{2\sqrt{\psi_{0x}/\pi}}{3G_1(\psi_{0x})}-\dfrac{2}{3\pi[G_1(\psi_{0x})]^2} & (x_0<x<x_r, v_x>0)\\[2ex] 1-\dfrac{2\sqrt{\psi_{nx}/\pi}}{3G_2(\psi_{nx})}-\dfrac{2}{3\pi[G_2(\psi_{nx})]^2} & (x_r<x<x_n),\end{cases} \tag{24}$$

and

$$Q=\frac{(2+\psi_{nx})n_0T_0e^{-\psi_{n0}}}{2\sqrt{\pi\beta}}. \tag{25}$$

III. PRESHEATH AND SHEATH DESCRIPTION

The relations describing plasma electrons, plasma ions, and surface-emitted electrons within the presheath and sheath are obtained directly from the expressions presented in Sec. II and are listed below. The notation used is as follows. Location subscripts: p—edge-plasma–presheath interface; b—presheath-sheath interface; m—electric potential minimum; r—the location in Fig. 2(c) where the electric potential equals that at x_p (x_r is not shown in Fig. 2); s—sheath-surface interface; and x—location along the x coordinate. Two adjacent location subscripts means the difference in values at the two locations. For example, $\phi_{ms}=\phi_m-\phi_s$. Particle subscripts: e—plasma electrons; i—plasma ions; and δ—surface-emitted electrons. Symbols: ϕ—the electric potential; e—the unit charge; and Z—the ion charge state. Definitions: $\beta_e=m_e/(2T_{pe})$; $\beta_i=m_i/(2T_{pi})$; $\beta_\delta=m_e/(2T_{s\delta})$; $\psi_e=U_e/T_{pe}=-e\phi/T_{pe}$; $\psi_i=U_i/T_{pi}=Ze\phi/T_{pi}$; and $\psi_\delta=U_\delta/T_{s\delta}=-e\phi/T_{s\delta}$.

Plasma electrons within the potential profile shown in Fig. 2(a) are described by

$$f_e(x,\mathbf{v})=n_{pe}\left(\frac{\beta_e}{\pi}\right)^{3/2}e^{-\beta_e v^2-\psi_{xpe}}\Theta\left(v_x+\left(\frac{\psi_{sxe}}{\beta_e}\right)^{1/2}\right), \tag{26}$$

$$n_e=\frac{1}{2}\,n_{pe}e^{-\psi_{spe}}G_2(\psi_{sxe}), \tag{27}$$

$$F_e=\frac{n_{pe}e^{-\psi_{spe}}}{2\sqrt{\pi\beta_e}}, \tag{28}$$

$$\frac{T_e}{T_{pe}}=1-\frac{2\sqrt{\psi_{sxe}/\pi}}{3G_2(\psi_{sxe})}-\frac{2}{3\pi[G_2(\psi_{sxe})]^2}, \tag{29}$$

and

$$Q_e=\frac{(2+\psi_{sxe})n_{pe}T_{pe}e^{-\psi_{spe}}}{2\sqrt{\pi\beta_e}}. \tag{30}$$

Plasma electrons within the potential profiles shown in Figs. 2(b) and 2(c) are described by

$$f_e(x,\mathbf{v})=\begin{cases}n_{pe}\left(\dfrac{\beta_e}{\pi}\right)^{3/2}e^{-\beta_e v^2-\psi_{xpe}}\Theta\left(v_x+\left(\dfrac{\psi_{mxe}}{\beta_e}\right)^{1/2}\right) & (x_p<x<x_m)\\[2ex] n_{pe}\left(\dfrac{\beta_e}{\pi}\right)^{3/2}e^{-\beta_e v^2-\psi_{xpe}}\Theta\left(v_x-\left(\dfrac{\psi_{mxe}}{\beta_e}\right)^{1/2}\right) & (x_m<x<x_s),\end{cases} \tag{31}$$

$$n_e=\begin{cases}\frac{1}{2}n_{pe}e^{-\psi_{mpe}}G_2(\psi_{mxe}) & (x_p<x<x_m)\\ \frac{1}{2}n_{pe}e^{-\psi_{mpe}}G_1(\psi_{mxe}) & (x_m<x<x_s),\end{cases} \tag{32}$$

$$F_e=\frac{n_{pe}e^{-\psi_{mpe}}}{2\sqrt{\pi\beta_e}}, \tag{33}$$

$$\frac{T_e}{T_{pe}}=\begin{cases}1-\dfrac{2\sqrt{\psi_{mxe}/\pi}}{3G_2(\psi_{mxe})}-\dfrac{2}{3\pi[G_2(\psi_{mxe})]^2} & (x_p<x<x_m)\\[2ex] 1+\dfrac{2\sqrt{\psi_{mxe}/\pi}}{3G_1(\psi_{mxe})}-\dfrac{2}{3\pi[G_1(\psi_{mxe})]^2} & (x_m<x<x_s),\end{cases} \tag{34}$$

and

$$Q_e=\frac{(2+\psi_{mxe})n_{pe}T_{pe}e^{-\psi_{mpe}}}{2\sqrt{\pi\beta_e}}. \tag{35}$$

Plasma ions within the potential profiles shown in Figs. 2(a) and 2(b) are described by

$$f_i(x,\mathbf{v})=n_{pi}\left(\frac{\beta_i}{\pi}\right)^{3/2}e^{-\beta_i v^2+\psi_{pxi}}\Theta\left(v_x-\left(\frac{\psi_{pxi}}{\beta_i}\right)^{1/2}\right), \tag{36}$$

$$n_i=\frac{1}{2}\,n_{pi}G_1(\psi_{pxi}), \tag{37}$$

$$F_i=\frac{n_{pi}}{2\sqrt{\pi\beta_i}}, \tag{38}$$

$$\frac{T_i}{T_{pi}}=1+\frac{2\sqrt{\psi_{pxi}/\pi}}{3G_1(\psi_{pxi})}-\frac{2}{3\pi[G_1(\psi_{pxi})]^2}, \tag{39}$$

and

$$Q_i=\frac{(2+\psi_{pxi})n_{pi}T_{pi}}{2\sqrt{\pi\beta_i}}. \tag{40}$$

Plasma ions within the potential profile shown in Fig. 2(c) are described by

$$f_i(x,v)=\begin{cases} n_{pi}\left(\frac{\beta_i}{\pi}\right)^{3/2}e^{-\beta_i v^2+\psi_{pxi}}\left[1-\Theta\left(v_x+\left(\frac{\psi_{pxi}}{\beta_i}\right)^{1/2}\right)\Theta\left(\left(\frac{\psi_{pxi}}{\beta_i}\right)^{1/2}-v_x\right)\right]\Theta\left(v_x+\left(\frac{\psi_{sxi}}{\beta_i}\right)^{1/2}\right) & (x_p<x<x_r) \\ n_{pi}\left(\frac{\beta_i}{\pi}\right)^{3/2}e^{-\beta_i v^2-\psi_{xpi}}\Theta\left(v_x+\left(\frac{\psi_{sxi}}{\beta_i}\right)^{1/2}\right) & (x_r<x<x_s), \end{cases} \tag{41}$$

$$n_i=\begin{cases} n_{pi}[G_1(\psi_{pxi})-\frac{1}{2}e^{-\psi_{spi}}G_1(\psi_{sxi})] & (x_p<x<x_r) \\ \frac{1}{2}n_{pi}e^{-\psi_{spi}}G_2(\psi_{sxi}) & (x_r<x<x_s), \end{cases} \tag{42}$$

$$F_i=\frac{n_{pi}e^{-\psi_{spi}}}{2\sqrt{\pi\beta_i}}, \tag{43}$$

$$\frac{T_i}{T_{pi}}=\begin{cases} 1+\frac{2\sqrt{\psi_{pxi}/\pi}}{3G_1(\psi_{pxi})}-\frac{2}{3\pi[G_1(\psi_{pxi})]^2} & (x_p<x<x_r, v_x>0) \\ 1-\frac{2\sqrt{\psi_{sxi}/\pi}}{3G_2(\psi_{sxi})}-\frac{2}{3\pi[G_2(\psi_{sxi})]^2} & (x_r<x<x_s), \end{cases} \tag{44}$$

and

$$Q_i=\frac{(2+\psi_{sxi})n_{pi}T_{pi}e^{-\psi_{spi}}}{2\sqrt{\pi\beta_i}}. \tag{45}$$

For the description of surface-emitted electrons, particle and energy fluxes are defined as positive in the negative-x direction. Surface-emitted electrons within the potential profile shown in Fig. 2(a) are described by

$$f_\delta(x,\mathbf{v})=n_{s\delta}\left(\frac{\beta_\delta}{\pi}\right)^{3/2}e^{-\beta_\delta v^2+\psi_{sx\delta}}\Theta\left(v_x-\left(\frac{\psi_{sx\delta}}{\beta_\delta}\right)^{1/2}\right), \tag{46}$$

$$n_\delta=\frac{1}{2}\,n_{s\delta}G_1(\psi_{sx\delta}), \tag{47}$$

$$F_\delta = \frac{n_{s\delta}}{2\sqrt{\pi\beta_\delta}}, \tag{48}$$

$$\frac{T_\delta}{T_{s\delta}} = 1 + \frac{2\sqrt{\psi_{sx\delta}/\pi}}{3G_1(\psi_{sx\delta})} - \frac{2}{3\pi[G_1(\psi_{sx\delta})]^2}, \tag{49}$$

and

$$Q_\delta = \frac{(2+\psi_{sx\delta})n_{s\delta}T_{s\delta}}{2\sqrt{\pi\beta_\delta}}. \tag{50}$$

Surface-emitted electrons within the potential profiles shown in Figs. 2(b) and 2(c) are described by

$$f_\delta(x,\mathbf{v}) = \begin{cases} n_{s\delta}\left(\dfrac{\beta_\delta}{\pi}\right)^{3/2} e^{-\beta_\delta v^2 - \psi_{xs\delta}} \Theta\left(v_x - \left(\dfrac{\psi_{mx\delta}}{\beta_\delta}\right)^{1/2}\right) & (x_p < x < x_m) \\ n_{s\delta}\left(\dfrac{\beta_\delta}{\pi}\right)^{3/2} e^{-\beta_\delta v^2 - \psi_{xs\delta}} \Theta\left(v_x + \left(\dfrac{\psi_{mx\delta}}{\beta_\delta}\right)^{1/2}\right) & (x_m < x < x_s), \end{cases} \tag{51}$$

$$n_\delta = \begin{cases} \frac{1}{2} n_{s\delta} e^{-\psi_{ms\delta}} G_1(\psi_{mx\delta}) & (x_p < x < x_m) \\ \frac{1}{2} n_{s\delta} e^{-\psi_{ms\delta}} G_2(\psi_{mx\delta}) & (x_m < x < x_s), \end{cases} \tag{52}$$

$$F_\delta = \frac{n_{s\delta} e^{-\psi_{ms\delta}}}{2\sqrt{\pi\beta_\delta}}, \tag{53}$$

$$\frac{T_\delta}{T_{s\delta}} = \begin{cases} 1 + \dfrac{2\sqrt{\psi_{mx\delta}/\pi}}{3G_1(\psi_{mx\delta})} - \dfrac{2}{3\pi[G_1(\psi_{mx\delta})]^2} & (x_p < x < x_m) \\ 1 - \dfrac{2\sqrt{\psi_{mx\delta}/\pi}}{3G_2(\psi_{mx\delta})} - \dfrac{2}{3\pi[G_2(\psi_{mx\delta})]^2} & (x_m < x < x_s), \end{cases} \tag{54}$$

and

$$Q_\delta = \frac{(2+\psi_{mx\delta})n_{s\delta}T_{s\delta}e^{-\psi_{ms\delta}}}{2\sqrt{\pi\beta_\delta}}. \tag{55}$$

Secondary electron emission occurs when an electron strikes a material surface and causes an ejection of one or more electrons from the surface. This emission process is characterized by the electron emission coefficient δ which equals the average ratio of electrons emitted from the surface to electrons incident on the surface. A relation for secondary electron emission suitable for a plasma-facing surface when space-charge saturation is not present within the sheath is [29]

$$\delta(T_{pe}) = \frac{2.6\delta_{\max}}{\sqrt{\pi r^3}} \int_0^\infty \frac{\epsilon^{7/6}(2+3\epsilon)e^{-\epsilon/r}}{(1+\epsilon)^2}\, d\epsilon, \tag{56}$$

where $r = 0.72T_{pe}/E_{\max}$, and $\delta_{\max}$ and $E_{\max}$ are material-dependent constants. (Values for $\delta_{\max}$ and $E_{\max}$ are found, for example, in Ref. [31].) When space-charge saturation is present within the sheath,

$$\delta(T_{pe},\psi_{mse}) = \frac{2.6\delta_{\max}e^{\psi_{mse}}}{\sqrt{\pi r^3}G_1(\psi_{mse})} \int_{r\psi_{mse}}^\infty \epsilon^{1/6} \times e^{-\epsilon/r}\left[\frac{3+4\sqrt{r\psi_{mse}\epsilon}}{(1+\sqrt{r\psi_{mse}\epsilon})^2} - \frac{3+4\epsilon}{(1+\epsilon)^2}\right] d\epsilon \tag{57}$$

provides a suitable relation for secondary electron emission [29].

The gross flux of emitted electrons at the material surface, $F_{g\delta}$, is given by Eq. (48). Consequently, the source density of surface-emitted electrons is

$$n_{s\delta} = 2\sqrt{\pi\beta_\delta}F_{g\delta}. \tag{58}$$

For secondary electron emission,

$$F_{g\delta} = \delta F_e, \tag{59}$$

where F_e is the net flux of plasma electrons (which is the same at any location with the presheath and sheath) striking the surface. Note that the return of secondary electrons to the surface within a space-charge saturated sheath is not considered to result in additional secondary electron emission. Only plasma electrons (which normally will have much larger energies) which strike the surface are considered to produce secondary electrons. For thermionic electron emission, the

gross electron flux leaving the surface is given by the Richardson-Dushman equation,

$$F_{g\delta}=AT_{s\delta}^2 e^{-\Phi/T_{s\delta}}, \tag{60}$$

where Φ is the work function of the plasma-facing surface at temperature $T_{s\delta}$ and A is a material-dependent constant. (Values for A are found, for example, in Ref. [32].) In order to use the same description for both secondary electron emission and thermionic electron emission, Eqs. (58) and (59) can be combined to give

$$n_{s\delta}=2\sqrt{\pi\beta_\delta}\delta F_e, \tag{61}$$

where, for thermionic electrons,

$$\delta=\frac{AT_{s\delta}^2 e^{-\Phi/T_{s\delta}}}{F_e} \tag{62}$$

should be used while for secondary electrons, Eqs. (56) and (57) are suitable.

IV. EVALUATION OF THE SHEATH AND PRESHEATH POTENTIALS

A number of conditions are implemented in order to evaluate the sheath and presheath potentials. The first two conditions are that the total current density to the electrically floating surface is zero (for a steady-state solution) and that the charge density at the presheath-sheath interface is zero. The third condition is that the spatial integral of the charge density in the presheath is zero. This requires the presheath to be globally quasineutral. It should be noted, however, that a manifestation of the presheath model used here is that the presheath is not locally quasineutral except at the presheath-sheath interface. The fourth condition, which applies only when space-charge saturation takes place within the sheath, is that the electric field at the electric potential minimum is zero.

The first condition, zero current density, requires $ZF_i=F_e-F_\delta$. With Eqs. (28), (33), (38), (43), (48), (53), and (61), this condition provides the relations

$$\alpha=e^{-\psi_{spe}}(1-\delta)\left(\frac{\eta}{\tau_i}\right)^{1/2}, \tag{63}$$

$$\alpha=e^{-\psi_{mpe}}(1-\delta e^{-\psi_{ms\delta}})\left(\frac{\eta}{\tau_i}\right)^{1/2}, \tag{64}$$

and

$$\alpha=e^{\psi_{spi}-\psi_{mpe}}(1-\delta e^{-\psi_{ms\delta}})\left(\frac{\eta}{\tau_i}\right)^{1/2}, \tag{65}$$

which correspond to the potential profiles shown in Figs. 2(a), 2(b), and 2(c), respectively. Here, $\alpha=Zn_{pi}/n_{pe}$ is a parameter called the neutralization factor [21], $\eta=m_i/m_e$, and $\tau_i=T_{pi}/T_{pe}$.

In order to implement the second and third conditions, the charge density $\rho=e(Zn_i-n_e-n_\delta)$ between x_p and x_b is needed. The charge density can be written as a set of three relations in terms of α corresponding to the three potential profiles using Eqs. (27), (28), (32), (33), (37), (42), (47), (52), and (61). Substituting for α the right-hand sides from Eqs. (63)–(65) provides

$$\frac{2\rho e^{\psi_{spe}}}{en_{pe}}=(1-\delta)\left(\frac{\eta}{\tau_i}\right)^{1/2}G_1(\psi_{pxi})-G_2(\psi_{sxe})-\frac{\delta}{\sqrt{\tau_\delta}}G_1(\psi_{sx\delta}), \tag{66}$$

$$\frac{2\rho e^{\psi_{mpe}}}{en_{pe}}=(1-\delta e^{-\psi_{ms\delta}})\left(\frac{\eta}{\tau_i}\right)^{1/2}G_1(\psi_{pxi})-G_2(\psi_{mxe})-\frac{\delta}{\sqrt{\tau_\delta}}e^{-\psi_{ms\delta}}G_1(\psi_{mx\delta}), \tag{67}$$

$$\frac{2\rho e^{\psi_{mpe}}}{en_{pe}}=(1-\delta e^{-\psi_{ms\delta}})\left(\frac{\eta}{\tau_i}\right)^{1/2}[2e^{\psi_{spi}}G_1(\psi_{pxi})-G_1(\psi_{sxi})]-G_2(\psi_{mxe})-\frac{\delta}{\sqrt{\tau_\delta}}e^{-\psi_{ms\delta}}G_1(\psi_{mx\delta}), \tag{68}$$

where $\tau_\delta=T_{s\delta}/T_{pe}$. The second condition, zero charge density at the presheath-sheath interface, requires the right-hand sides of the above relations to equal zero at x_b. This is written as

$$(1-\delta)\left(\frac{\eta}{\tau_i}\right)^{1/2}G_1(\psi_{pbi})=G_2(\psi_{sbe})+\frac{\delta}{\sqrt{\tau_\delta}}G_1(\psi_{sb\delta}), \tag{69}$$

$$(1-\delta e^{-\psi_{ms\delta}})\left(\frac{\eta}{\tau_i}\right)^{1/2}G_1(\psi_{pbi})=G_2(\psi_{mbe})+\frac{\delta}{\sqrt{\tau_\delta}}e^{-\psi_{ms\delta}}G_1(\psi_{mb\delta}), \tag{70}$$

and

$$(1-\delta e^{-\psi_{ms\delta}})\left(\frac{\eta}{\tau_i}\right)^{1/2}[2e^{\psi_{spi}}G_1(\psi_{pbi})-G_1(\psi_{sbi})]=G_2(\psi_{mbe})+\frac{\delta}{\sqrt{\tau_\delta}}e^{-\psi_{ms\delta}}G_1(\psi_{mb\delta}). \tag{71}$$

The third condition, that the spatial integral of the charge density in the presheath is zero, requires zero electric fields at x_p and x_b. With no electric fields at the edge-plasma–presheath interface and at the presheath-sheath interface, it can be shown [see, for example, Eq. (36) of Ref. [22]] that $\int_{\phi_p}^{\phi_b}\rho d\phi=0$ or, equivalently, $\int_{\psi_{pe}}^{\psi_{be}}\rho d\psi_{xe}=0$. Consequently, with Eqs. (66)–(68), the third condition requires

$$(1-\delta)\left(\frac{\eta}{\tau_i}\right)^{1/2}\int_{\psi_{pe}}^{\psi_{be}} G_1(\psi_{pxi})\,d\psi_{xe}=\int_{\psi_{pe}}^{\psi_{be}} G_2(\psi_{sxe})\,d\psi_{xe}+\frac{\delta}{\sqrt{\tau_\delta}}\int_{\psi_{pe}}^{\psi_{be}} G_1(\psi_{sx\delta})\,d\psi_{xe}\,, \tag{72}$$

$$(1-\delta e^{-\psi_{ms\delta}})\left(\frac{\eta}{\tau_i}\right)^{1/2}\int_{\psi_{pe}}^{\psi_{be}} G_1(\psi_{pxi})\,d\psi_{xe}=\int_{\psi_{pe}}^{\psi_{be}} G_2(\psi_{mxe})\,d\psi_{xe}+\frac{\delta}{\sqrt{\tau_\delta}}\,e^{-\psi_{ms\delta}}\int_{\psi_{pe}}^{\psi_{be}} G_1(\psi_{mx\delta})\,d\psi_{xe}\,, \tag{73}$$

$$(1-\delta e^{-\psi_{ms\delta}})\left(\frac{\eta}{\tau_i}\right)^{1/2}\left[2e^{\psi_{spi}}\int_{\psi_{pe}}^{\psi_{be}} G_1(\psi_{pxi})\,d\psi_{xe}-\int_{\psi_{pe}}^{\psi_{be}} G_1(\psi_{sxi})\,d\psi_{xe}\right]$$

$$=\int_{\psi_{pe}}^{\psi_{be}} G_2(\psi_{mxe})\,d\psi_{xe}+\frac{\delta}{\sqrt{\tau_\delta}}\,e^{-\psi_{ms\delta}}\int_{\psi_{pe}}^{\psi_{be}} G_1(\psi_{mx\delta})\,d\psi_{xe}\,. \tag{74}$$

Since the electric field is zero at the presheath-sheath interface, the fourth condition, which requires the electric field at the electric potential minimum to be zero, is equivalent to requiring the spatial integral of the charge density between the presheath-sheath interface and the potential minimum to be zero. Hence the fourth condition is similar to the third except that it applies only to the profiles shown in Figs. 2(b) and 2(c) and that it applies between x_b and x_m. Using Eqs. (67) and (68) for the charge density between x_b and x_m, the fourth condition requires

$$(1-\delta e^{-\psi_{ms\delta}})\left(\frac{\eta}{\tau_i}\right)^{1/2}\int_{\psi_{be}}^{\psi_{me}} G_1(\psi_{pxi})\,d\psi_{xe}=\int_{\psi_{be}}^{\psi_{me}} G_2(\psi_{mxe})\,d\psi_{xe}+\frac{\delta}{\sqrt{\tau_\delta}}\,e^{-\psi_{ms\delta}}\int_{\psi_{be}}^{\psi_{me}} G_1(\psi_{mx\delta})\,d\psi_{xe}\,, \tag{75}$$

$$(1-\delta e^{-\psi_{ms\delta}})\left(\frac{\eta}{\tau_i}\right)^{1/2}\left[2e^{\psi_{spi}}\int_{\psi_{be}}^{\psi_{me}} G_1(\psi_{pxi})\,d\psi_{xe}-\int_{\psi_{be}}^{\psi_{me}} G_1(\psi_{sxi})\,d\psi_{xe}\right]$$

$$=\int_{\psi_{be}}^{\psi_{me}} G_2(\psi_{mxe})\,d\psi_{xe}+\frac{\delta}{\sqrt{\tau_\delta}}\,e^{-\psi_{ms\delta}}\int_{\psi_{be}}^{\psi_{me}} G_1(\psi_{mx\delta})\,d\psi_{xe}\,. \tag{76}$$

The integrals in Eqs. (72)–(76) are given by the two indefinite integrals

$$\int G_1(x)\,dx=G_1(x)+2\left(\frac{x}{\pi}\right)^{1/2} \tag{77}$$

and

$$\int G_2(x)\,dx=G_2(x)-2\left(\frac{x}{\pi}\right)^{1/2} \tag{78}$$

along with $\psi_i=-Z\psi_e/\tau_i$ and $\psi_\delta=\psi_e/\tau_\delta$. The electric potential at one location must also be defined. Hereafter, the electric potential at the presheath-sheath interface shall be defined as zero, $\psi_{be}=0$. With $\psi_{be}=0$, ψ_{se} gives the normalized sheath potential drop (as a positive value for a monotonically decreasing potential) and ψ_{pe} gives the normalized presheath potential drop (as a negative value). For a monotonically decreasing potential [Fig. 2(a)], Eqs. (69) and (72) are solved simultaneously for the two unknown parameters, ψ_{pe} and ψ_{se}. For a space-charge saturated sheath, the three unknown parameters, ψ_{pe}, ψ_{me}, and ψ_{se} are solved simultaneously using Eqs. (70), (73), and (75) if the surface has a negative floating potential with respect to the edge plasma and Eqs. (71), (74), and (76) if the surface has a positive floating potential. In order to determine the transition from the potential profile in Fig. 2(a) to that in Fig. 2(b) (this transition occurs at the onset of space-charge saturation), Eqs. (70), (73), and (75) are solved simultaneously for δ, ψ_{pe}, and ψ_{se} under the condition $\psi_{me}=\psi_{se}$. In order to determine the transition from the potential profile in Fig. 2(b) to that in Fig. 2(c), Eqs. (70), (73), and (75) are solved simultaneously for δ, ψ_{pe}, and ψ_{me} under the condition $\psi_{se}=\psi_{pe}$.

Once the values for the normalized potentials are known, the profile of the electric potential within the presheath and sheath is evaluated using Poisson's equation. The procedure is outlined in Ref. [22]. Equation (39) of Ref. [22] is written here as

$$\frac{x}{\lambda_{D(p)}}=\int_{\psi_{pe}}^{\psi_{xe}}\left[\int_{\psi'_{pe}}^{\psi'_{xe}}\frac{2\rho(\psi''_{xe})}{en_{pe}}\,d\psi''_{xe}\right]^{-1/2}d\psi'_{xe}$$

$$(x_p<x<x_m), \tag{79}$$

where $x_p=0$, $\lambda_{D(p)}$ is the Debye length in the edge plasma, and $2\rho(\psi''_{xe})/(en_{pe})$ is given by Eqs. (66)–(68). The inner integral of this relation is evaluated in closed form while the outer is evaluated numerically. The results are then inverted to obtain ψ_{xe} as a function of x. Figure 2 shows actual self-consistent calculations of different electric potential profiles. [The vertical dimensions are different for each of the three profiles shown in Fig. 2. The horizontal dimensions are the same, however, and the width of the curve in Fig. 2(a) is $27\lambda_{D(p)}$]. The profiles are calculated for a thermal ($\tau_i=1$) hydrogen ($Z=1,\eta=1836$) plasma which is bounded by an electron-emitting surface (with $\tau_\delta=0.2$). The profiles are shown in order of increasing values for the electron emission coefficient: $\delta=0$ for Fig. 2(a), $\delta=15$ for Fig. 2(b), and

$\delta=1000$ for Fig. 2(c). The values for the normalized potentials calculated for each of the profiles are $\psi_{pe}=-0.34$ and $\psi_{se}=2.5$ for Fig. 2(a); $\psi_{pe}=-0.43$, $\psi_{me}=0.29$, and $\psi_{se}=-0.28$ for Fig. 2(b); and $\psi_{pe}=-0.53$, $\psi_{me}=0.31$, and $\psi_{se}=-1.1$ for Fig. 2(c). The onset of space-charge saturation occurs at $\delta=0.88$, $\psi_{pe}=-0.43$, and $\psi_{me}=\psi_{se}=0.29$ while the transition from a negative to a positive surface floating potential occurs at $\delta=31$, $\psi_{pe}=\psi_{se}=-0.43$, and $\psi_{me}=0.29$.

V. BOUNDARY CONDITIONS

The boundary conditions provided in this section are those which occur at the presheath-sheath interface. This location is both quasineutral and electric-field-free. For brevity, location subscripts are not used in this section since quantities which were previously location dependent are now only considered at the presheath-sheath interface. The boundary conditions at the presheath-sheath interface are the pressure terms $\langle v_y^2\rangle$, $\langle v_z^2\rangle$, and $\langle v_x^2\rangle-\langle v_x\rangle^2$, the plasma flow velocity $\langle v_x\rangle$, and the energy flow term $\langle v^2 v_x\rangle$. Using relations from Sec. III, the boundary conditions are written in terms of the electron and ion plasma temperatures (T_e and T_i) at the presheath-sheath interface, the temperature (T_δ) associated with electrons emitted at the plasma-facing surface, the ratio (τ_i) of ion to electron plasma temperatures at the edge plasma, the normalized presheath (ψ_{pe}), sheath (ψ_{se}), and minimum (ψ_{me}) potentials, the electron and ion masses (m_e and m_i), and the ion charge state (Z). Using relations in Sec. IV, the normalized potentials are evaluated numerically and the values obtained are fit in terms of Z, τ_i, the electron emission coefficient (δ), which equals the ratio of surface-emitted electron flux to plasma electron flux incident on the surface, the ratio (η) of ion-to-electron mass, and the ratio (τ_δ) of the temperature associated with electrons emitted at the surface to the electron plasma temperature at the edge plasma. Of the three types of electric potential profiles shown in Fig. 2, the third is expected to be rare since, for $\tau_\delta\leqslant 0.1$, the electron emission coefficient must be very large, $\delta>10^3$, to produce the type of potential profile shown in Fig. 2(c) (with $\tau_i\sim 1$). For this reason, only boundary conditions for the electric potential profiles shown in Figs. 2(a) and 2(b) are presented. Also, all calculations of normalized potentials are carried out using the same τ_δ value, $\tau_\delta=0.01$. This is appropriate since, for $\tau_\delta\leqslant 0.1$, the normalized potentials are essentially independent of τ_δ.

For use of the boundary conditions, τ_i is the only nonlocal parameter needed. The value for τ_i should be evaluated at one of two possible locations depending on which of the two has a shorter path length to the wall surface (the path length should be along a magnetic field line if a magnetic field is present). One location is an ion mean free path away from the wall surface while the other location is where the maximum temperature occurs along the magnetic field line. The first of these two locations applies when no magnetic field is present or when the source of presheath ions is predominantly either ionization or diffusion parallel to a magnetic field; the second method applies when diffusion perpendicular to a magnetic field provides most of the presheath ions.

Two of the boundary conditions, the second and third pressure terms, can be written in terms of another boundary condition, the first pressure term. They are $\langle v_z^2\rangle=\langle v_y^2\rangle$ and

$$\langle v_x^2\rangle-\langle v_x\rangle^2=\frac{3T}{m}-2\langle v_y^2\rangle. \tag{80}$$

The other boundary conditions are determined separately for plasma electrons, plasma ions, and surface-emitted electrons. (For surface-emitted electrons, $\langle v_x\rangle_\delta$ and $\langle v^2 v_x\rangle_\delta$ are defined as positive in the negative-x direction.) For the electric potential profile shown in Fig. 2(a), the boundary conditions are

$$\langle v_y^2\rangle_e=\frac{T_e}{m_e\chi_{se}}, \tag{81}$$

$$\langle v_x\rangle_e=\frac{\sqrt{2\langle v_y^2\rangle_e/\pi}}{e^{\psi_{se}}\mathrm{erfc}(-\sqrt{\psi_{se}})}, \tag{82}$$

$$\langle v^2 v_x\rangle_e=2(2+\psi_{se})\langle v_y^2\rangle_e\langle v_x\rangle_e, \tag{83}$$

$$\langle v_y^2\rangle_i=\frac{T_i}{m_i\chi_{pi}}, \tag{84}$$

$$\langle v_x\rangle_i=\frac{\sqrt{2\langle v_y^2\rangle_i/\pi}}{e^{\psi_{pi}}\mathrm{erfc}(\sqrt{\psi_{pi}})}, \tag{85}$$

$$\langle v^2 v_x\rangle_i=2(2+\psi_{pi})\langle v_y^2\rangle_i\langle v_x\rangle_i, \tag{86}$$

$$\langle v_y^2\rangle_\delta=\frac{T_\delta}{m_e}, \tag{87}$$

$$\langle v_x\rangle_\delta=\frac{\sqrt{2\langle v_y^2\rangle_\delta/\pi}}{e^{\psi_{s\delta}}\mathrm{erfc}(\sqrt{\psi_{s\delta}})}, \tag{88}$$

and

$$\langle v^2 v_x\rangle_\delta=2(2+\psi_{s\delta})\langle v_y^2\rangle_\delta\langle v_x\rangle_\delta, \tag{89}$$

where the following definitions are used:

$$\chi_{se}=1-\frac{2\sqrt{\psi_{se}/\pi}}{3e^{\psi_{se}}\mathrm{erfc}(-\sqrt{\psi_{se}})}-\frac{2}{3\pi[e^{\psi_{se}}\mathrm{erfc}(-\sqrt{\psi_{se}})]^2}$$
$$\approx\ln(2.51\psi_{se}^{0.042}), \tag{90}$$

$$\chi_{pi}=1+\frac{2\sqrt{\psi_{pi}/\pi}}{3e^{\psi_{pi}}\mathrm{erfc}(\sqrt{\psi_{pi}})}-\frac{2}{3\pi[e^{\psi_{pi}}\mathrm{erfc}(\sqrt{\psi_{pi}})]^2}$$
$$\approx\ln(2.05\psi_{pi}^{-0.013}), \tag{91}$$

$\psi_{pi}=-Z\psi_{pe}/\tau_i$, and $\psi_{s\delta}=T_e\psi_{se}/(T_\delta\chi_{se})$. The approximations for χ_{se} and χ_{pi} are accurate to within 2% for $0.1<\psi_{se}<10$ and $0.01<\psi_{pi}<100$, respectively. For the normalized sheath and presheath potentials, the following two expressions are recommended:

$$\psi_{se}=\ln[0.2725(1-\delta)\sqrt{\eta}\tau_i^{-0.092}Z^{-0.44}], \tag{92}$$

$$\psi_{pe}=-\ln\left[1.43\left(\frac{Z}{\tau_i}\right)^{0.195}\right]. \tag{93}$$

These expressions are fits to numerically determined values using the values 1, 10, and 100 times the proton-to-electron mass ratio (1836) for η; $\frac{1}{3}$, 1, and 3 for τ_i; 1, 2, and 3 for Z; and 0 and $\frac{1}{2}$ for δ. The numerically determined values were calculated using all possible combinations of η, τ_i, Z, and δ except combinations which simultaneously involved $Z>1$ and $\eta=1836$. The expressions for ψ_{se} and ψ_{pe} agree to within 4% and 7%, respectively, with the numerically determined values. Notice that the relation for the sheath potential has the usual $\ln[(1-\delta)\sqrt{\eta}]$ dependence given elsewhere [33,34].

The onset of space-charge saturation and the corresponding transition from a monotonically decreasing potential [e.g., Fig. 2(a)] to a potential profile with a potential minimum [e.g., Fig. 2(b)] takes place if the electron emission coefficient reaches a sufficiently large value. A suitable expression which provides the value of the electron emission coefficient at the transition between profiles is

$$\delta_c = 1 - 7.7\tau_i^{0.1}\left(\frac{Z}{\eta}\right)^{1/2}. \tag{94}$$

This expression is a fit to values determined numerically for the same combinations of η, τ_i, and Z which were used for the ψ_{se} and ψ_{pe} fits. The δ_c fit is remarkably accurate, being within 0.1% of the numerically determined values.

If the electron emission coefficient, as determined using Eq. (56), for example, is larger than δ_c, boundary conditions associated with the potential profile shown in Fig. 2(b) should be used. For the potential profile shown in Fig. 2(b), the boundary conditions are the same as those for Fig. 2(a) except with subscript s replaced by subscript m. For the normalized sheath minimum and presheath potentials under space-charge saturation conditions [Fig. 2(b)], the following two expressions are recommended:

$$\psi_{me} = \ln(1.63\eta^{0.01}) \tag{95}$$

and

$$\psi_{pe} = -\ln\left[1.51\left(\frac{Z}{\tau_i}\right)^{0.209}\right]. \tag{96}$$

These two expressions agree to within 5% and 6%, respectively, with numerically determined values using the combinations of η, τ_i, and Z used for the δ_c fit along with $\delta=\delta_c$ and 10. Note that these expressions are independent of δ for $\delta \geqslant \delta_c$. Thus a specific relation for the electron emission coefficient under conditions of space-charge saturation [e.g., Eq. (57)] is not needed for calculating the associated boundary conditions. It should also be mentioned that trapping of slow charge-exchange ions within the potential well surrounding the potential minimum has been found to be responsible for reducing space-charge saturation [30]. When that is the case, it is probable that the sheath potential profile is adequately described by using an effective electron emission coefficient which is smaller than the actual one. If so, then for situations in which $\delta > \delta_c$, the boundary conditions presented here are unaffected by ion trapping since the sheath minimum and presheath potentials are not dependent on δ. Nevertheless, a more detailed study of the effects of ion trapping on space-charge saturation appears warranted.

VI. DISCUSSION AND CONCLUDING SUMMARY

It is illustrative to consider the limit imposed on the net surface-emitted electron current density as a result of space-charge saturation. This limit is traditionally calculated using the Child-Langmuir equation [35]

$$J_{\mathrm{CL}} = \frac{4}{9}\left(\frac{2e}{m_e}\right)^{1/2}\left(\frac{\epsilon_0 V^{3/2}}{d^2}\right). \tag{97}$$

The Child-Langmuir equation is derived considering a planar electron-emitting cathode situated a distance d from a planar anode in vacuum. The magnitude of the potential difference between the cathode and anode is V. The derivation is carried out employing a zero-electric-field boundary condition at the cathode surface. This boundary condition occurs at the onset of space-charge saturation. The Child-Langmuir equation can be applied to a plasma sheath adjacent to an electrically floating surface by setting V equal to the sheath potential and d equal to a few Debye lengths [36]. This requires substituting $V=-\phi_s=T_{pe}\psi_{se}/e$ and $d=N\lambda_{D(p)}=N(\epsilon_0 T_{pe}/n_{pe}e^2)^{1/2}$ into Eq. (97). The result is

$$J_{\mathrm{CL}} = \frac{4}{9N^2}\left(\frac{2T_{pe}}{m_e}\right)^{1/2} e n_{pe}\psi_{se}^{3/2}. \tag{98}$$

A relation which can be compared with Eq. (98) is derived by combining Eqs. (33), (53), and (61). Using $J_\delta = eF_\delta$, the net current density of surface-emitted electrons traveling away from the surface is

$$J_\delta = \frac{1}{2\sqrt{\pi}}\left(\frac{2T_{pe}}{m_e}\right)^{1/2} e n_{pe}\delta e^{-(\psi_{me}/\tau_\delta - \psi_{se}/\tau_\delta + \psi_{me} - \psi_{pe})}. \tag{99}$$

At the onset of space-charge saturation, $\delta=\delta_c$ and $\psi_{se}=\psi_{me}$. With δ_c, ψ_{me}, and ψ_{pe} given by Eqs. (94)–(96) and using the same combinations of values for η, τ_i, and Z as used for the fits, Eqs. (98) and (99) are found to agree to within 37% for $N=1.6$. This value for N is about half the value ($N=3$) used in Ref. [36]. The agreement between Eqs. (98) and (99) for the spectrum of values used for η, τ_i, and Z is indicative of the weak dependence δ_c, ψ_{me}, and ψ_{pe} have on η, τ_i, and Z under space-charge saturation conditions.

Because the sheath theory developed in the present work only considers an electrically floating plasma-facing material surface, it is not suitable for evaluating the current limit due to space-charge saturation for a current-carrying cathode. Other limitations of the present work are associated with the simplifying assumptions used. For example, the effect of a magnetic field is not taken into account. Consequently, for use with magnetized plasmas, the boundary conditions presented in Sec. V are suited to situations where the magnetic field intersects a plasma-facing surface at normal incidence. This is not typically the case (e.g., for fusion plasmas) and a future extension of the theory is needed which incorporates the effect of a magnetic field which has an oblique incidence. Another limitation of the present work is associated with low-temperature plasmas where large numbers of charge-exchange reactions can occur in the edge plasma and where a variety of ion masses can simultaneously exist. Both of these effects can influence particle and energy transport through

the presheath and sheath. If these two effects can be ignored, then the boundary conditions given by Eqs. (81)–(89) with the normalized presheath and sheath potentials given by Eqs. (92) and (93) should be suitable for low-temperature plasmas where small values of the electron emission coefficient exist ($\delta < \delta_c$). For a situation where plasma flows parallel to the plasma-facing surface, two conditions are necessary for the boundary conditions to be suitable for use. First, the ion thermal speed should be much larger than the plasma flow speed. Second, the time scale over which plasma parameters change adjacent to a plasma-facing material surface as a result of the plasma flow should be much larger than the sheath time scale given by the inverse electron plasma frequency. It should be mentioned that the utility of the boundary conditions presented in Sec. V shall be more thoroughly explored once they are incorporated into a computer program which simulates plasma processes [37].

In summary, a fully kinetic self-consistent theory capable of describing the plasma sheath under conditions of space-charge saturation has been presented. The phase-space distribution functions for each species of particles have been evaluated and velocity moments have been taken in order to obtain particle densities, fluxes, temperatures, and energy fluxes. The electric potential profile has been determined self-consistently for three different types of profiles. These are a monotonically decreasing potential, a single-minimum potential associated with a negative surface floating potential, and a single-minimum potential associated with a positive surface floating potential. The electron emission requirements for production of the third potential profile were found to be severe. For this reason, boundary conditions have been provided only for the first two of the three potential profiles. Boundary conditions on velocity moments have been supplied for three separate species: plasma electrons, plasma ions, and surface-emitted electrons. These boundary conditions can be combined as needed for use in multifluid and single-fluid (MHD) applications. The boundary conditions are in terms of sheath and presheath potential drops and simple expressions have been provided for these potential drops. Once the potential drop expressions are inserted into the boundary conditions, the boundary conditions are in terms of the three species' temperatures, τ_i, the ion-to-electron plasma temperature ratio, Z, the ion charge state, η, the ion-to-electron mass ratio, and δ, the electron emission coefficient.

In order to determine the value of δ at which the transition between the first two potential profiles occurs, the following expression was developed: $\delta_c = 1 - 7.7\tau_i^{0.1}\sqrt{Z/\eta}$. This expression gives the value of the electron emission coefficient at the onset of space-charge saturation. For $\delta < \delta_c$, the following expressions are recommended for the sheath and presheath potentials normalized to the electron-plasma temperature: $\ln[0.2725(1-\delta)\sqrt{\eta}\tau_i^{-0.092}Z^{-0.44}]$ and $\ln[1.43(Z/\tau_i)^{0.195}]$. For $\delta \geqslant \delta_c$, recommended expressions for the normalized sheath minimum and presheath potentials are, respectively, $\ln(1.63\eta^{0.01})$ and $\ln[1.51(Z/\tau_i)^{0.209}]$. The conditions these expressions for δ_c and the normalized potential are expected to be suitable for are a temperature associated with the emitted electrons which is less than one-tenth that associated with the plasma electrons; $1/3 \leqslant \tau_i \leqslant 3$; $1 \leqslant Z \leqslant 3$; and $1836 \leqslant \eta \leqslant 100 \times 1836$.

ACKNOWLEDGMENTS

The author would like to thank Dr. R. E. Peterkin, Jr. of the Air Force Phillips Laboratory for helpful discussions. This work was supported by the Air Force Office of Scientific Research.

[1] X. Zhai, E. Garate, R. Prohaska, A. Fisher, and G. Benford, Phys. Lett. A **186**, 330 (1994).
[2] P. J. Turchi, in *Space Propulsion Analysis and Design*, edited by R. W. Humble, G. N. Henry, and W. J. Larson (McGraw-Hill, New York, 1995), p. 509.
[3] S. Fasoulas, P. C. Sleziona, M. Auweter-Kurtz, H. A. Habiger, S. H. Laure, and A. T. Schonemann, J. Thermophys. Heat Transfer **9**, 422 (1995).
[4] R. E. Peterkin, Jr., J. H. Degnan, T. W. Hussey, N. F. Roderick, and P. J. Turchi, IEEE Trans. Plasma. Sci. **21**, 522 (1993).
[5] M. L. Ramalingam, U.S. Air Force Wright Laboratory Report No. WL-TR-92-2004, 1992 (unpublished).
[6] J. Mathew, R. F. Fernsler, R. A. Meger, J. A. Gregor, D. P. Murphy, R. E. Pechacek, and W. M. Manheimer, Phys. Rev. Lett. **77**, 1982 (1996).
[7] T. Wagner, E. Eberl, K. Frank, W. Hartmann, D. H. H. Hoffmann, and R. Tkotz, Phys. Rev. Lett. **76**, 3124 (1996).
[8] J. R. Marques, J. P. Geindre, F. Amiranoff, P. Audebert, J. C. Gauthier, A. Antonetti, and G. Grillon, Phys. Rev. Lett. **76**, 3566 (1996).
[9] C. W. Siders, S. P. Le Blanc, D. Fisher, T. Tajima, M. C. Downer, A. Babine, A. Stepanov, and A. Sergeev, Phys. Rev. Lett. **76**, 3570 (1996).
[10] P. Sortais, Rev. Sci. Instrum. **67**, 867 (1996).
[11] M. Sekiguchi, Rev. Sci. Instrum. **67**, 1606 (1996).
[12] G. Ondrey and K. Fouhy, Chem. Eng. **98**, 32 (1991).
[13] *Proceedings of the 7th Symposium on Electromagnetic Launch Technology* [IEEE Trans. Magn. **31** (1995)].
[14] V. R. Malghan, Energy Convers. Mgmt. **37**, 569 (1996).
[15] M. Kenward, Phys. World **8**, 31 (1995).
[16] D. B. Graves, IEEE Trans. Plasma Sci. **22**, 31 (1994).
[17] J. Sheffield, Rev. Mod. Phys. **66**, 1015 (1994).
[18] J. V. Shebalin, J. Spacecr. Rockets **28**, 394 (1991).
[19] D. E. Hastings, J. Geophys. Res. **100**, 14 457 (1995).
[20] C. A. Ordonez, Phys. Plasmas **1**, 1359 (1994).
[21] L. A. Schwager and C. K. Birdsall, Phys. Fluids B **2**, 1057 (1990).
[22] C. A. Ordonez, Phys. Fluids B **4**, 778 (1992).
[23] L. A. Schwager, Phys. Fluids B **5**, 631 (1993).
[24] K. Kurihara, Y. Kiwamoto, T. Saito, K. Yatsu, and S. Miyoshi, J. Phys. Soc. Jpn. **61**, 3153 (1992).
[25] T. Saito, Y. Kiwamoto, K. Kurihara, T. Cho, M. Inutake, S. Miyoshi, T. Tamano, and K. Yatsu, Phys. Fluids B **5**, 866 (1993).
[26] Y. Tatematsu, Y. Kiwamoto, T. Saito, and T. Tamano, J. Phys. Soc. Jpn. **63**, 558 (1994).

[27] Y. Tatematsu, Y. Kiwamoto, T. Saito, Y. Yoshimura, T. Takahashi, I. Katanuma, M. Inutake, and T. Tamano, J. Nucl. Mater. **220-222**, 575 (1995).
[28] T. Saito, Y. Kiwamoto, Y. Tatematsu, Y. Yoshimura, T. Takahashi, M. Inutake, and T. Tamano, Phys. Plasmas **2**, 352 (1995).
[29] C. A. Ordonez and R. E. Peterkin, Jr., J. Appl. Phys. **79**, 2270 (1996).
[30] T. Intrator, M. H. Cho, E. Y. Wang, N. Hershkowitz, D. Diebold, and J. DeKock, J. Appl. Phys. **64**, 2927 (1988).
[31] E. W. Thomas, in *Data Compendium for Plasma-Surface Interactions*, special issue of Nucl. Fusion **1984**, 94.
[32] K. Ertl and R. Behrisch, in *Physics of Plasma-Wall Interactions in Controlled Fusion*, edited by D. E. Post and R. Behrisch (Plenum, New York, 1986), p. 515.
[33] P. C. Stangeby, in *Physics of Plasma-Wall Interactions in Controlled Fusion*, edited by D. E. Post and R. Behrisch (Plenum, New York, 1986), p. 41.
[34] R. N. Franklin and W. E. Han, Plasma Phys. Control. Fusion **30**, 771 (1988).
[35] I. Langmuir and K. T. Compton, Rev. Mod. Phys. **3**, 191 (1931).
[36] M. Y. Ye, S. Masuzaki, K. Shiraishi, S. Takamura, and N. Ohno, Phys. Plasmas **3**, 281 (1996).
[37] The boundary conditions presented in Sec. V are to be incorporated into the Air Force multidimensional MHD program, MACH.